All-round: combining laser cutting and edge shaping of glass

David Sohr, Jens Ulrich Thomas, Stefan Skupin

All-Round: Combining laser cutting and edge shaping of glass

David Sohr[1,2*], Jens Ulrich Thomas[2] and Stefan Skupin[1]

[1*]Institut Lumière Matière, UMR 5306 Université Lyon 1 - CNRS, Université de Lyon, 69622 Villeurbanne, France.
[2]SCHOTT AG, Hattenbergstrasse 10, 55122 Mainz, Germany.

*Corresponding author(s). E-mail(s): david.sohr@univ-lyon1.fr;

Abstract

Cutting glass to shape with ultra short laser pulses is nowadays a well established industrial process. Pulses with an elongated straight focal volume (line focus) are used to modify the workpiece throughout its entire depth with one single laser shot. At the same time, processed glass is often required to have a seamed or round edge, which usually requires an extra grinding step. Here we demonstrate that curved line foci can be used to combine cutting and edge shaping of glass sheets in one laser process. We reconsider the Airy-Gauss beam for this purpose, and suggest modifications to the beam profile to avoid unwanted effects, in particular an asymmetric laser modification of the glass sheet. We provide a combined experimental and numerical analysis of the laser process, and show a symmetric convex edge created in a 920 µm thick glass sheet.

Keywords: Airy beams, Borosilicate glass, Beam shaping, Laser materials processing, Numerical analysis

1 Introduction

Glass is one of the most important materials when it comes to modern integrated devices [1–3], and intense ultrashort pulsed (USP) lasers have been widely adapted as tool for industrial glass cutting throughout the past years. They are particularly useful tools because laser energy absorption is highly nonlinear at these high intensities, which makes the machining process precisely controllable. Undesired thermal effects can be largely avoided because of the ultrashort interaction times [4]. In particular when the laser pulses are tightly focused, the deposited energy density is highly localized, and can induce stresses as well as irreversible volume modifications [5]. However, for glass cutting elongated interaction volumes are necessary, because the material modification needs to penetrate the total material thickness. Therefore, ultra short pulse lasers with their beams shaped to produce an elongated focal volume (line focus) like, e.g., the non-diffractive Bessel beam [6], are typically used for USP laser cutting processes, which are increasingly replacing conventional cutting tools [7, 8].

USP laser cutting processes make use of the possibility of creating weakened zones within the glass volume along which the sheet can be separated in a subsequent process. The geometry of the weakened zone and the extent of damage that is created by a single laser pulse depends on the focal intensity distribution of the laser beam and on the choice of laser parameters for a given substrate. The focal intensity distribution of the aforementioned optical Bessel beam is quasi invariant over propagation distances far greater than its transversal extent and exhibits a high contrast between the main lobe and the side lobes. For

these reasons this beam has been widely studied and optimized and is probably the most commonly used one for glass cutting. When it comes to single pass laser glass cutting, the thickness of the glass sheet is in principle only limited by two factors, namely the size of the optics and the laser pulse energy [9, 10]. The cutting process itself is based on creating permanent modifications in the material, reaching from structural changes to voids and cracks. Thus, the laser affected zones are weakened compared to the pristine material. In order to be able to separate the glass by, e.g., mechanical cleaving or etching, many of these weakened zones are created with a constant lateral shift, the so-called pitch. Single pass laser glass cutting generally results in straight, vertical edges, and has been demonstrated for glass thicknesses up to 12 mm [8].

For many applications, however, glass sheets with convex, seamed or rounded egdes are required. Most importantly the convex edge leads to an increased durability and better positioning at mechanical stops during further processing of the sheet. In addition a convex edge also improves handling safety as cutting hazards are reduced. Nowadays the edge shaping is usually achieved by a separate mechanical grinding step after the cutting process. Curved laser focus geometries as for example produces by the Airy-Gauss beam provide a new tool for combining cutting and edge shaping and produce convex “c-cut” edges as a direct result of the cutting process [11] when used in the aforementioned micromachining setup.

A characteristic feature of the non linear propagation of the unmodified Airy-Gauss beam in glass is the preferential energy deposition in front of the linear focus, which leads to an asymmetric edge that has its apex beneath the center of the glass sheet and thus is effectively tilted with respect to the sheet [11]. After revisiting these first experimental cutting results with the Airy-Gauss beam, we will present numerical simulation results that help to identify the origin of this preferential energy deposition. Subsequently we propose modifications the optical setup that can compensate for this effect of preferential absorption. With this compensation, we demonstrate a curved, symmetric edge after etching.

2 Using Airy-Gauss beams for glass cutting

The Airy beam is the most prominent example of a non diffracting beam that follows a curved trajectory along its propagation. Equivalently the beam is said to accelerate in the transverse plane during propagation. The Airy beam was first theoretically described in 1979 [12], and a physical realization of the optical, finite-energy Airy-Gauss beam featuring a curved line focus was first demonstrated in 2007 [13]. Various beam shaping concepts based on the Airy beam have been proposed, reaching from 1D light sheets [14] to light bullets formed by a ring-Airy [15]. The most commonly treated case, however, is still the 2D case given by the linear combination of cubic phases along two perpendicular axes in the conjugated Fourier plane [16–18]. The 2D Airy beam is the first of a whole group of accelerating beams [19] and has been used before to create long, curved plasma channels in air [18] and for micromachining of thin sheets of diamond and silicon [16]. It is important note, however, that the ”curved trajectory” or any ”accelerating beam” is just a result of diffraction continuously changing the beam profile during propagation. The center of mass of the whole intensity distribution always follows a straight line [13], as follows from the conservation quantities belonging to the wave equation. It is only the main lobe of the beam profile that appears to be accelerated in the transverse plane during propagation.

2.1 Setup for the Airy-Gauss beams

The Airy beam profile, like the Bessel beam profile, is not normalizable and formally requires infinite power. Therefore, in experiments it is always attenuated at large distances from the center lobe. Quite naturally, this can be achieved with a large Gaussian envelope. Here, we will briefly recapitulate the paraxial description of the propagation of such an Airy-Gauss beam, as proposed and used in previous publications [11, 13, 18].

The Airy-Gauss beam is produced by adding a cubic phase $\exp[\mathrm{i}\beta^3(x^3/3 + xy^2)/\sqrt{2}]$ with a scale factor β to a Gaussian input beam with optical wavelength λ and half beam width (at $1/\mathrm{e}^2$ intensity) w_0. The complex electric field envelope behind a focusing optical element with an effective

focal length f is then characterized by the transverse length scale factor $x_0 = \sqrt{2}f\beta/k$, the dimensionless longitudinal coordinate $\zeta = 2z/(kx_0^2)$, the confinement factor $a = 1/(w_0^2\beta^2)$, and can be expressed as [13]

$$E(\zeta, x, y) = \mathrm{Ai}\left(\frac{x-y}{x_0} - \frac{\zeta^2}{4} + \mathrm{i}a\zeta\right) \mathrm{Ai}\left(\frac{x+y}{x_0} - \frac{\zeta^2}{4} + \mathrm{i}a\zeta\right) \mathrm{e}^{a\left(2x/x_0 - \zeta^2\right) - \mathrm{i}\zeta\left(\zeta^2/6 + a^2 + x/x_0\right)}. \quad (1)$$

The curved focal line to be used for micromachining is defined by the main lobe of the complex field envelope $E(\zeta, x, y)$, which maintains an intensity exceeding $1/\mathrm{e}^2$ of its maximum over a length $l \approx 2w_0 f^2\beta^3/k$. The quadratic coefficient $q = 1/(k^2x_0^3)$ that describes the parabolic trajectory of the main lobe in the xz plane can also be expressed in terms of an effective bending radius $r = k^2x_0^3/2$. This quadratic offset along the propagation is often referred to as an acceleration of the main lobe. Equivalently, the angle α between the optical axis and the line focus is given by $\alpha(z) = \arctan(2qz)$.

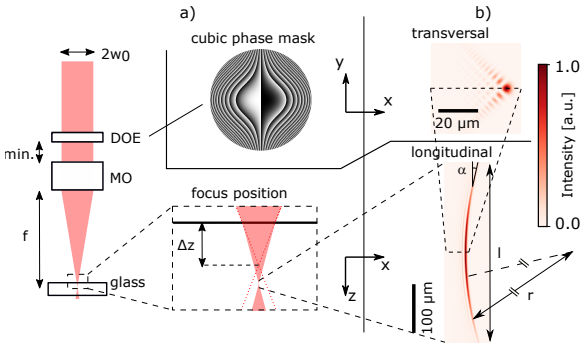

Fig. 1 Experimental 2f-setup (left) used for creating an Airy-Gauss beam [11] (see text for details) and intensity profiles (right) according to Eq. (1) for $f = 10\,\mathrm{mm}$. Throughout the paper, the focus position is given as the shift Δz of the glass surface with respect to the focus position in air (dotted line).

Such an Airy-Gauss beam can be readily produced as the focal image of a beam with a cubic phase. The required cubic phase can be imprinted by a specifically designed phase mask, such as a diffractive optical element (DOE), a spatial light modulator (SLM) or cylindrical lenses [14, 20, 21]. For all our micro machining experiments we used a diffractive optical element (DOE: Airy Beam Generator, Holo/Or, 9 mm clear aperture diameter) as phase mask. In the first experimental setups aspherical lenses (Thorlabs AL1210, AL1225, AL2018) were used as focussing optics. These, however, did not produce the expected Airy focal line and the resulting glass modifications exhibited unwanted artefacts. In particular, we observed distortions that arise due to spherical aberration. To avoid these distortions in further experiments we used a microscope objective (MO, Trumpf TopCleave, two different models with focal lengths 10 mm and 20 mm respectively) as focusing optics as shown in Fig. 1. We estimated the position of the front focal plane by illuminating the rear side of the MO with a collimated beam and measuring the beam diameter behind the MO. We found that the front focal plane of the MO lies within the housing of the MO, but the DOE could not be placed exactly at this plane. Rather the DOE has been placed as close to the MO as the mechanical parts allowed (effective distance 4 mm). With this setup we confirmed that the intensity profiles produced with the microscope objective match the expected propagation behaviour of the Airy-Gauss beam in air. The focal lengths of 10 mm and 20 mm and the cubic phase β that was fixed at $3^{1/3}\ \mathrm{mm}^{-1}$ by the DOE, yield an effective bending radius in air of 0.70 mm and 5.6 mm respectively.

In the micro machining experiments we used an integrated industrial laser machine with a laser center wavelength $\lambda = 1030\,\mathrm{nm}$, an input beam radius w_0 of 2.65 mm, and a pulse duration t_p tunable between 1 ps and 10 ps to structure sheets of borosilicate glass (SCHOTT Borofloat® 33), also see [11] for more details. The pulses in the burst mode all have the same energy and pulse duration and are separated by an intra burst period of 25 ns.

The Airy beam propagation was first characterized by inspecting the ablation pattern at the glass surface for various distances between focusing optics and glass sheet by moving the focusing optics along z. The focus position was then defined as the half-way position within the depth range in which an ablation pattern is observed. For a symmetric longitudinal intensity distribution, which is expected for the Airy beam, this corresponds to the position, for which the maximum intensity lies at the surface of the glass sheet. The focus position was thus determined to an accuracy of 50 µm. Decreasing the distance between the focusing optics and the glass sheet by a defined distance Δz then leads to a focus position of $n\Delta z$ beneath the surface (see Fig. 1) in linear propagation. As the orientation of the DOE could only roughly be adjusted by the lens tube system, the ablation pattern was also used to determine the orientation of the Airy profile. The lateral translation in the xy plane was then adjusted to ensure that the cutting lines are perpendicular to the acceleration direction of the beam, thus maximising the curvature of the cross section profile. Along the cutting lines, discrete modifications were produced by picking single laser pulses. This way the distance between neighbouring modifications, also referred to as pitch, could be kept at constant values of 10, 25 or 50 µm respectively. Various combinations of pulse duration, burst mode, pulse energy, focus position and pitch were used during the experiments.

2.2 Airy-Gauss volume modifications

By placing the focus deeply within a 6.5 mm thick glass sheet ($\Delta z = 2$ mm) we avoided discontinuum effects such as plasma ignition at the surface. The profile of the resulting volume modifications were charaterized by looking vertically along a line of modifications in reflected light microscopy (Keyence VHX 6000). For these profile measurements we took special care to avoid double shots by synchronizing the laser shutter with the internal phase of the laser source during pulse picking.

Straightforwardly, the length and the lateral extent of the modifications both increase with increasing pulse energy, while the curvature remains unchanged and is in good agreement with

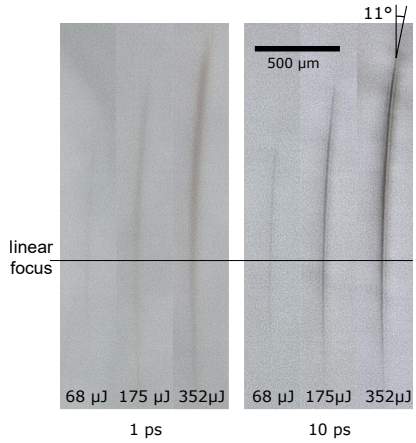

Fig. 2 Light microscopy cross sections of permanent in-volume modifications produced by focusing an Airy-Gauss beam with focal length $f = 20$ mm in glass. The modifications follow a parabolic trajectory which agrees well with the expected profile given by Eq. (1). Note the increase in length with pulse energy, the much more confined and pronounced modification for longer pulse durations and the preferential energy deposition in front of the linear focus.

the theoretically expected value. At a pulse energy of 352 µJ we reach lengths of up to 2 mm and a maximum angle $a_{max} = 11°$ for $f = 20$ mm, see Fig. 2. We also observe that the modifications are broad and indistinct for 1 ps pulses and more confined and stronger modifications are observed for longer pulse durations. In linear propagation we would expect the damage to be symmetrically distributed around its focus. We observe, however, that the modifications are shifted towards to laser source relative to the linear focus position. In part this can be attributed to a slight misalignment of the Gaussian input beam. This effect we have made use of in further experiments and it will be discussed in detail in Sec. 4. This misalignment, however, would only tilt and shift the volume modification, but we also observe an increasingly asymmetric damage distribution along the parabola with increasing pulse energy, with the most extensive damage shifted towards the laser source and a long tail away from it, an effect which also has been observed for the relative balance of modifications at top and bottom surface in thin sheets, see Sec. 2.3. This can be understood in terms of the non linear interaction between glass and laser pulse, which we have studied in more detail by means of numerical simulations, see Sec. 3.

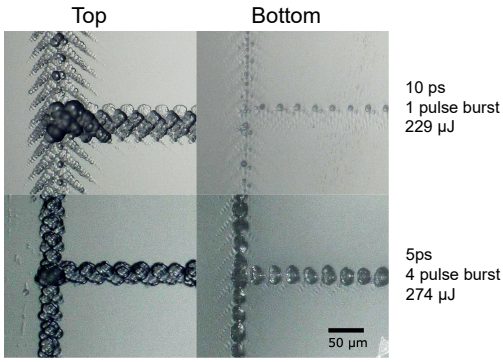

Fig. 3 Light microscopy views of permanent modifications at the top and bottom surface after etching with potassium hydroxide for a short time, equivalent to 10 µm removal at each side. Pulse configurations are indicated in the figure.

2.3 Surface effects and etching behaviour

For a single pass laser process, i.e. a process that perforates the full thickness of a glass sheet with one laser shot, the modification has to extend up to both surfaces. In particular the interaction between the laser pulse and the top surface therefore needs to be considered as well, as it may change the further propagation of the laser pulse.

To further characterize the asymmetry of the energy deposition along the beam path, we thus examined top and bottom surface modifications for various combinations of pulse duration, burst mode, and pulse energy. In a first step the modifications at top and bottom were inspected right after the laser process. In a further step, the glass sheets were etched simultaneously from both top and bottom surface with potassium hydroxide [22] for a short time, equivalent to 10 µm removal at each side of the pristine sheet ("etching radius"). For further details of the etching process see [23] and the supplementary material of [11]. The etching step thus helps to show weak modifications that would not be visible with the light microscope. Some exemplary results are shown in Fig. 3 for a 1 mm thick glass sheet and $f = 20$ mm. The ideal case would be surface modifications that are identical in extent and lateral position, indicating a setting with both good penetration and a symmetric position within the glass sheet. Due to the absorption and defocusing by the electron plasma and the resulting asymmetry however, the bottom modification was suppressed if visible at all for symmetric beam positioning. With the additional

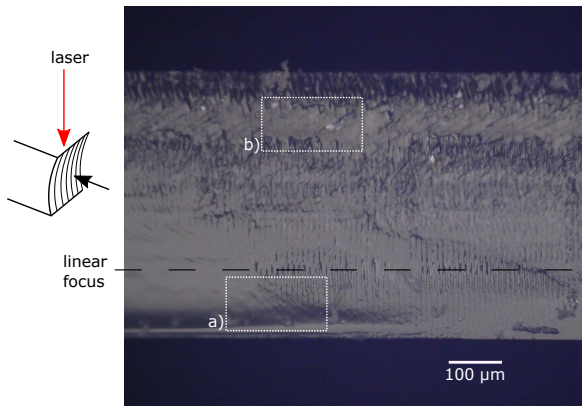

Fig. 4 Side view onto concave side of a glass sheet cleaved mechanically after laser perforation with $E_{burst} = 428$ µJ from the top as shown on the left [11]. Note the larger areas of concoidal fracture (a) for which in some parts the modifications can be seen through the smoothly fractured glass that is building up on the concave side. A continuous zone of concoidal fracture below the top surface (b) has been interpreted as shadow zone due to plasma ignition at the surface.

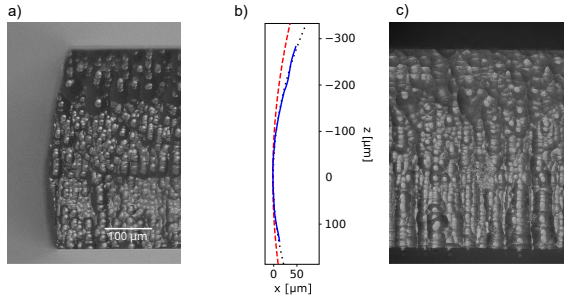

Fig. 5 Result of cutting a 525 µm thick glass sheet by perforation with an Airy beam and subsequent etching (50 µm etching depth) [11]. A cross section view (a) parallel to the line of laser modifications shows the curved profile of the cut. The average height profile (b) measured by confocal light microscopy (solid blue) and its parabolic fit (dotted black) exhibit a considerably stronger curvature than the Airy profile (dashed red), which can be attributed to the etching process. The side view onto the convex side (c) shows a coarser structure at the bottom, probably due to less extensive damage leading to more localized etching.

etching step, modifications at the bottom surface become visible as well. Clearly, passing to intermediate pulse durations and separating the energy into bursts helps to reduce the asymmetry in the damage between top and bottom surface.

Another aspect to consider is the overlap of neighbouring modifications. Especially for long pulses the overlapping region of the Airy side lobes tends to show a larger etching rate than the

main lobe modification, cf. Fig. 3, which again can be explained by enhanced avalanche ionization at defects for long pulses. We also observe that large numbers of pulses in the burst are not favourable for the process. Modifications written with 4 pulse bursts show stronger cracking with poorly defined directions compared to those created with an intermediate 2 pulse burst. While the dependence of avalanche ionization on pre-existing defects puts a limit on the pulse duration, the same physical process seems to be responsible for an optimum at intermediate pulse numbers. Again, the low focal contrast exacerbates this effect, as volumes that should not be damaged are exposed to relatively high intensities. In the case of separation by mechanical cleaving, cf. Fig. 4, this can deviate the crack away from the intended cutting line, during etching this can mean that the curvature of the resulting edge is reduced, cf. Fig. 5.

2.4 Separation results

Our separation results [11] obtained by mechanical cleaving and wet etching after laser processing with a 2D Airy-Gauss beam are shown in Fig. 4 and Fig. 5 respectively. In both cases a focal length of 10 mm and a 2 pulse burst with $t_p = 5\,\mathrm{ps}$ has been used. Mechanical cleaving along the perforated surface could only be achieved on small segments along the intended cutting surface and the crack in many places deviated from this surface, often cutting short into the convex side. On such mechanically cleaved edges we also observed a continuous zone of smooth concoidal fracture ca. 90 µm beneath the top surface, which we interpreted as a shadow zone caused by a plasma ignited at the surface in the side lobes of the beam. By examining both surface and volume modification for bursts of 1 to 4 of pulses and pulse durations of 1 to 10 ps in reflected and transmitted light micropscopy we identified a burst of 2 pulses, each with a duration of 5 ps, as the optimum within our parameter range, see [11] for more details.

Wet etching on the other hand lead to successful separation with a well defined, parabolic edge. However, to ensure a modification throughout the full thickness of the sheet while keeping unwanted damage in the side lobes sufficiently small we had to position the linear focus beneath the center of the glass sheet, resulting in an asymmetric edge. In Sec. 4 we present the adaptations of the Airy beam that we used to compensate the asymmetry to achieve a symmetric edge.

3 Numerical simulation of the energy deposition

The asymmetry observed in the volume modifications can be understood in terms of the non linear propagation within the glass [11]. Here, we present in more detail the unidirectional pulse propagation model accounting for all relevant nonlinear propagation effects, in particular the laser-generated conduction electrons [24, 25].

3.1 Model

The ultrashort laser pulse propagation in the glass and related energy deposition can be described by an extended nonlinear optical Schrödinger equation [25]. Key ingredients to capture the highly nonlinear progagation dynamics are the optical Kerr effect leading to self-focusing, and ionization yielding conduction electrons and therefore light defocusing [24]. For the particular case of Airy beams, the latter effect is dominant, and is also responsible for the transfer of laser energy into the glass matrix. The slowly varying complex optical field envelope $\mathcal{E}(x, y, \bar{t}, z)$ is governed by the following equation:

$$\partial_z \mathcal{E} = \frac{\mathrm{i}}{2k_0}\left(\frac{\partial^2}{\partial x^2} + \frac{\partial^2}{\partial y^2}\right)\mathcal{E} - \mathrm{i}\frac{k''}{2}\partial_{\bar{t}}^2\mathcal{E} - \frac{\sigma}{2}N_e\mathcal{E} + \mathrm{i}\frac{\omega_0 n_2}{c}I\mathcal{E} - \mathrm{i}\frac{k_0}{2n_0^2 N_c}N_e\mathcal{E} - \frac{E_g W_{PI}(N_{nt} - N_e)}{2I}\mathcal{E}\,. \quad (2)$$

Table 1 Material parameters used for simulation of SCHOTT Borofloat® 33, cf. [7]

n_0	1.5	σ [cm^2]	1.1×10^{-18}
n_2 [cm^2/W]	5.7×10^{-16}	τ_c [fs]	20
E_g [eV]	4.3	τ_{rec} [fs]	150
k'' [fs^2/cm]	250	N_{nt} [cm^{-3}]	2.1×10^{22}
N_c [cm^{-3}]	1.0×10^{21}		

In this equation, linear material dispersion is taken into account up to the second order group velocity dispersion k'', and n_0 and n_2 are the linear and nonlinear refractive indexes, respectively. The group velocity itself does not appear explicitly, as it is hidden in the retarded time variable $\bar{t}$, that is, the whole model is formulated in a frame moving with the group velocity of the pulse at center frequency ω_0 and wave number $k_0 = n_0\omega_0/c$. The optical field envelope is normalized such that $I = |\mathcal{E}|^2$, where I is the laser pulse intensity, N_c is the critical electron density in the conduction band, and E_g is the band gap energy. The inverse Bremsstrahlung cross section $\sigma = k_0 e^2\tau_c/[n_0^2\omega_0\varepsilon_0 m_e(1+\omega_0^2\tau_c^2)]$ is derived from a simple Drude model, where τ_c is the effective electron collision time. The evolution of the electron density in the conduction band $N_e(x, y, \bar{t}, z)$ reads

$$\partial_{\bar{t}} N_e = W_{\mathrm{PI}}\,(N_{nt} - N_e) + N_e\frac{\sigma I}{E_g} - \frac{N_e}{\tau_{\mathrm{rec}}}\,, \qquad (3)$$

where N_{nt} is the initial density of valence electrons, W_{PI} is the photo-ionization rate derived from Keldysh formula [26], and τ_{rec} is the time scale on which the electrons effectively return to a bound state in the dielectric material. This includes fast mechanisms such as the self-trapping of excitons, which has been observed on time scales of 150 fs in fused silica [27]. All relevant material parameters used (if not stated otherwise) in the upcoming simulations are summarized in Table 1. As input condition for the laser pulses we employ the field at the upper sample surface computed by means of Fourier optics and free space (vacuum) propagation. Solving Eqs. (2) and (3) gives access to the local energy loss of the laser field and thus to the spatial distribution of deposited laser energy density $\rho_{\mathrm{V}}(x, y, z)$.

3.2 Numerical simulation results

Considering the result of the numerical simulations we first note that while the total energy deposition was larger for short pulses with $t_p = 1$ ps respectively, the energy density was much higher for the longer pulses with $t_p = 10$ ps for all pulse energies considered, see Fig. 6. This is also in agreement with previous observations obtained by pump-probe experiments [28] with Gaussian focusing. For the short pulses the laser affected zone is much broader. This can be attributed to an effect termed intensity clamping [29, 30], which leads to a lower energy confinement. This corroborates the experimental observation of more confined and stronger modifications for the 10 ps-pulses in Fig. 6.

Also the preferential energy deposition in front of the focus observed in the experiments is well captured by our simulations. It can be explained by nonlinear absorption due to generation of an electron plasma in the side lobes of the Airy beam, which is clearly visible for the high energy cases for both pulse durations shown in Fig. 6. The energy losses of the pulse versus propagation distance correspond to the energy per volume that is deposited within the material, integrated over each transversal slice respectively, giving thus a line density of deposited energy. The asymmetry seen for this line energy density distribution strongly depends on the choice of the effective electron collision time τ_c, as shown in Fig. 7 (b). This is in line with previous statement that the asymmetry is principally caused by plasma effects. Typical literature values of the effective electron collision time are in the low fs regime [31], with a rather large uncertainty. In fact, already assuming a constant collision time is a rather crude approximation. Nevertheless, the sensitivity of the deposited energy density on the collision time τ_c in our model can be used to constrain this parameter. Assuming that the line energy density scales linearly with the extent of damage that we see in microscope cross section, we compared the experimentally observed morphology of the Airy beam in combination with our non-linear simulations and found a rather good quantitative agreement for $\tau_c = 20$ fs, also see Fig. 7. This value was used for all further simulations, also for the results shown in Fig. 6.

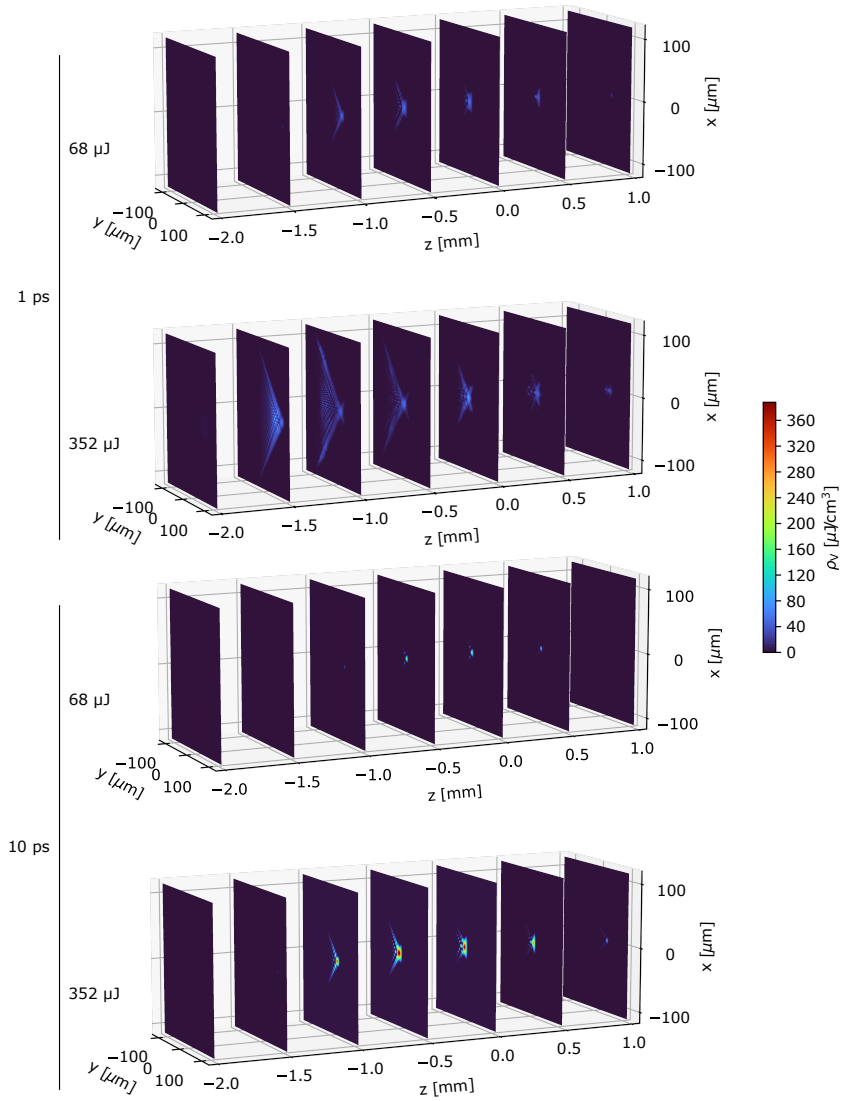

Fig. 6 Simulated energy densities for an Airy beam produced with $f = 20\,\text{mm}$ around the linear focus at $z = 0$ [11]. The four series of tomographically stacked transversal sections correspond to the highest and lowest pulse duration and pulse energy shown in Fig. 2 respectively.

Another non linear effect that could potentially cause a shift towards the laser source is the optical Kerr effect. The peak powers of the pulse configurations shown in Fig. 6 exceed the critical power for self-focusing, so that this effect could generally be expected to be relevant. We performed simulations without the term for self-focusing for the four cases shown in Fig. 6 to test the influence of the Kerr effect on the propagation and the resulting energy density distribution. A direct comparison as shown in Fig. 8 indicates that for 10 ps the Kerr effect causes only a slightly increased energy deposition and confinement for the long pulse duration, but the effect is small compared to the non linear propagation effects that arise from the plasma dynamics. This is plausible, because the linear focusing conditions lead to phase curvatures that are large compared those caused by the changes in the refractive index. We can therefore conclude that the asymmetry and shift towards the laser source in the distribution of deposited energy along the propagation are practically exclusively caused by plasma effects.

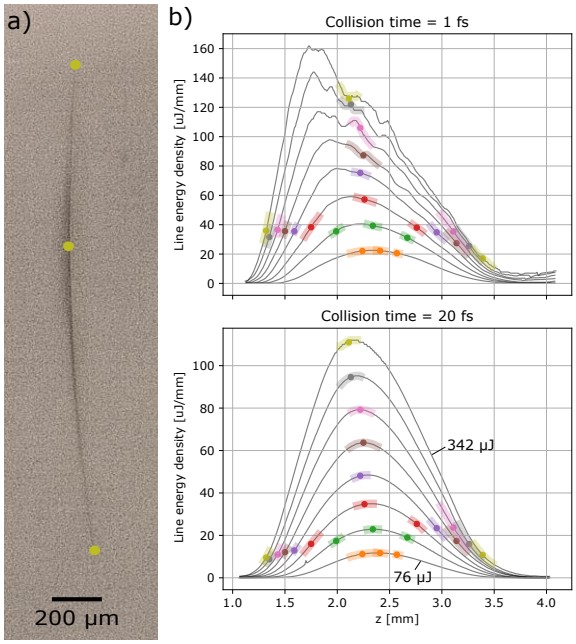

Fig. 7 Longitudinal cross section of volume modification (a) for $f = 20\,\text{mm}$, $t_p = 10\,\text{ps}$ and $E_p = 342\,\text{J}$ with the ends and the maximum indicated by yellow dots. These characteristic points are also marked on the graphs of the energy loss or line density of deposited energy (b) for various pulse energies and two values of the assumed effective electron collision time. The error of determining the position on the microscope image is shown as a broad bar. The longer collision time $\tau_c = 20\,\text{fs}$ yields good agreement, with the energy density at the ends being nearly constant across all pulse energies and the energy density maxima occurring at the positions of maximum damage.

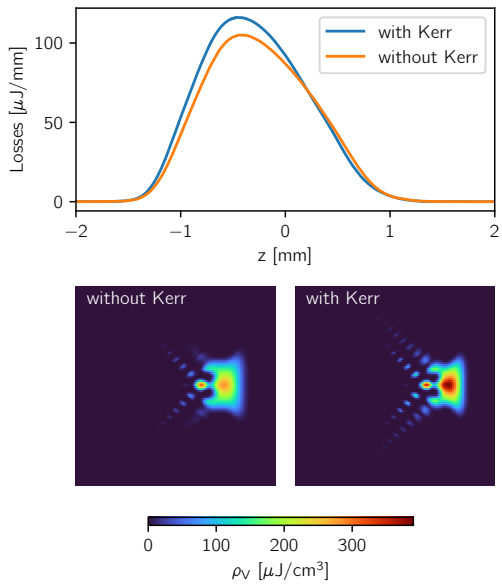

Fig. 8 Simulated energy deposition by a 10 ps pulse with 352 μJ energy (same pulse as shown in Fig. 6) with and without taking into account the Kerr effect, that is, the term $\propto I\mathcal{E}$ in Eq. (2). The upper panel shows the line density of deposited energy, the two lower panels show the deposited energy densities in the focal plane.

The highest plasma density reached our simulations, observed at a pulse duration of 1 ps, is $7 \times 10^{19}\,\text{cm}^{-3}$.

Overall, the observations of the volume modifications and the non linear simulations indicates that longer pulses are favorable for cutting applications. Another way to enhance the laser energy deposition in the bulk is to use the laser in burst mode operation [7], which we considered for the separation experiments.

4 Modified Airy-Gauss beams for glass cutting

So far we demonstrated that the 2D Airy-Gauss beam can be used to create curved volume modifications with lengths up to mm range in borosilicate glass and that these modifications can be used for glass cutting. However, these modifications suffer in particular from the low focal contrast of the Airy beam and the resulting excessive damage in the upper part and suppressed modification extent in the lower part of the glass sheet. For the application in glass cutting this poses a challenge by requiring an fine tuning of the laser parameters to the processed glass substrate and even then results in an asymmetric edge. Importantly, this also limits the achievable elevation contrast of the edge and the processable glass thickness.

Here we will present a strategy for compensating or overcoming these limitations of the Airy beam. To this end, we will consider the effect of low order aberrations that can be easily - and potentially dynamically - induced in the optical setup, leading to a shifted focal Airy intensity distribution, and that allow us to correct for the asymmetric non linear energy deposition and the resulting tilt.

4.1 Tilted Airy

The preferential energy deposition of the Airy (see Sec. 2.2) that leads to an asymmetric expression of the edge can be compensated, at least partly,

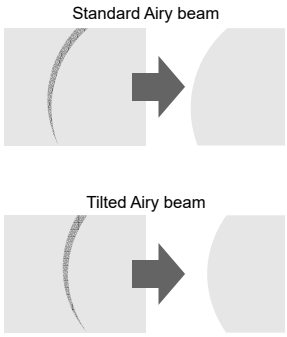

Fig. 9 Schematic representation of processing idea for creating symmetric edge by compensating preferential energy deposition by using a tilted Airy beam.

by tilting the Airy beam, as shown in Fig. 9. The Airy beam offers a convenient method for adding the required tilt on the focal line by what has previously been called "ballistic control" [32]. Hu et al. consider as two degrees of freedom for this control the transversal translation of the Gaussian input beam and the phase mask respectively. Intriguingly, the offset of the Gaussian beam input beam seems to shift the focal intensity distribution along the parabolic trajectory of the Airy beam. Aiming to understand if this is indeed an inherent property of the Airy beam and to quantify the amount of tilt that we can expect, we will examine the effect of an offset on the 2f setup before moving on to the application of the shifted beam in micromachining.

Moving a finite beam on an optical element is equivalent to changing to a shifted coordinate system with respect to the optical phase that is imprinted on the beam by the optical element. We will first consider the aberrations that arise in this new coordinate system for a 2D cubic phase mask, cf. Sect. 2.1, in paraxial approximation. Expanding the 2D cubic phase $\phi(x,y) = \beta^3(x^3/3 + xy^2)/\sqrt{2}$ for a shifted coordinate system $x = x' + x_{\mathrm{off}}$, i.e. an offset along its symmetry plane, yields

$$\begin{aligned}\phi(x' + x_{\mathrm{off}}, y) = \phi(x', y) + x' \frac{\beta^3 {x_{\mathrm{off}}}^2}{\sqrt{2}} \\ + r^2 \frac{x_{\mathrm{off}}\beta^3}{\sqrt{2}} + \frac{x_{\mathrm{off}}^3\beta^3}{3\sqrt{2}}\,,\end{aligned} \tag{4}$$

with $r^2 = x'^2 + y^2$. The phase term linear in x' induces a tilt of $\theta = \beta^3 {x_{\mathrm{off}}}^2/(\sqrt{2}k_0)$ behind the phase mask. We find that this term is negligible compared to the tilt x_{off}/f that arises from the same offset on an ideal thin parabolic lens with focal length f when $x_{\mathrm{off}} \ll \sqrt{2}k_0/(f\beta^3)$, i.e. for $x_{\mathrm{off}} < 1\,\mathrm{cm}$ with $\lambda = 1030\,\mathrm{nm}$, $f = 10\,\mathrm{mm}$ and $\beta = 3^{1/3}\mathrm{mm}^{-1}$.

The quadratic phase term $\propto r^2$ in Eq. 4 leads to defocussing by the phase mask with an effective focal length $f_1 = k_0/(x_{\mathrm{off}}\beta^3\sqrt{2})$. Simple geometrical combination of the focal powers of phase mask and microscope objective yields a new focal length

$$f' = \left(\frac{1}{f} + \frac{x_{\mathrm{off}}\beta^3\sqrt{2}}{k_0}\right)^{-1} \approx f\left(1 + \frac{f x_{\mathrm{off}}\beta^3\sqrt{2}}{k_0}\right) \tag{5}$$

which gives a focal shift

$$\Delta f = f' - f \approx \frac{f^2 x_{\mathrm{off}}\beta^3\sqrt{2}}{k_0}\,. \tag{6}$$

We checked the validity of the geometrical combination of the two focusing optical elements with the formalism of Gaussian optics [33], and found that for our parameters ($d = f$, $w_0 = 2.65\,\mathrm{mm}$) the results of geometrical and Gaussian optics agree very well and the defocus is indeed adequately described by Eq. (6). By considering the unique mapping of a point on the phase mask to a point along the Airy focal line [17, 34] one can see that an offset x_{off} does not impact the position of the maximum Airy lobe in the transverse plane and the intensity distribution is indeed simply shifted along a common parabolic trajectory when the Gaussian input beam is offset transversally.

Importantly, for the offset along the 2D Airy symmetry plane, as considered in Eq. (4), there is no astigmatic focus term, meaning that the intensity distribution will merely be translated and shifted and keep a constant lateral morphology. An offset along the normal of the symmetry axis on the other hand leads to an astigmatic defocus, which results in different focal planes along the 1D Airy profiles, thus giving a 1D Airy focus that transforms to another, orthogonally oriented 1D Airy focus along the propagation. This second case we will not further consider here.

4.2 Micromachining methods and results

With only minor adjustments of the original optical setup, as shown in Fig. 10, a shifted version

Table 2 Relative defocus and angles of shifted Airy volume modifications shown in Fig. 12. The measurements are made using modifications b) and c) due to uncertainty in the x_{off} value for modification a). Relative error of theoretical values ±10% due to the limited accuracy of adjusting x_{off}. The theoretical values are adjusted for the refractive index n of the glass, so that $\theta_{\text{glass}} = \theta/n$ and $\Delta f_{\text{glass}} = n\Delta f$.

	Defocus [μm]	Angle [°]
Theoretical	72	2.8
Measured	71	2.5

of the parabolic Airy focal line can be produced due to both tilt and defocus that result from the lateral offset on the optical elements. The ablation patterns at the glass surface were used to determine the new focus position and to check the alignment of the offset direction with the phase mask, see Fig. 11. We found that also for the tilted Airy cases the ablation pattern with the largest extent occurs in the middle of the z-range in which modifications are visible, i.e. there is no significant distortion. Figure 12 shows the volume modifications for various values of x_{off}. Piezo electric adjusters were used for the active mirror, which resulted in low repeatability and a poorly defined initial state (Fig. 12 a), but additional recording of the beam position with an inline beam camera enabled an position accuracy ca. ±10% for all further data. The defocus and tilt can clearly be seen and agree very well with the theoretically expected values, see Tab. 2. The length of the modifications remains nearly constant, as would be expected.

As a more controllable way to increase the uniformity of the intensity distribution along the propagation, we use an additional x2 beam

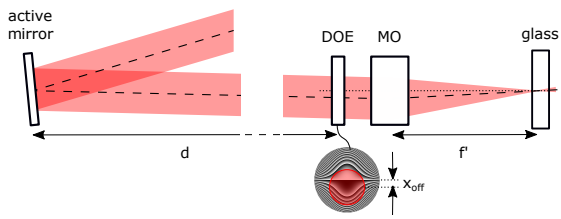

Fig. 10 Optical setup from Fig. 1 with additional degree of freedom to create a shifted Airy-Gauss beam. A small tilt early in the optical path ($d \approx 3$ m) effectively introduces a lateral offset x_{off} of the Gaussian input beam with respect to the diffractive optical element (DOE) and microscope objective (MO). Note that the offset beam is still centered on the mirror plane of the cubic phase mask.

expander to fully illuminate the DOE (9 mm clear aperture diameter) with a 10 mm diameter Gaussian input beam. We use an increased burst energy of 300 µJ to achieve sufficiently strong modifications while the other laser parameters remain the same as for previous successful separation experiments with the standard 2D Airy-Gauss beam in Sec. 2.4. For this set of parameters we find that a lateral offset x_{off} of 770 µm compensates the asymmetric energy deposition. Such an offset corresponds to a tilt of the Airy beam by 3° in glass.

We place the resulting modifications, that have a length of ca. 800 µm, at the center of a sheet of borosilicate glass (SCHOTT Borofloat® 33) that is 920 µm thick. This way we avoid complications due to the lower damage threshold at the surface [35]. Additionally, we choose a pitch that is suffiently large to avoid overlap between neighbouring modifications.

4.3 Separation results

In a subsequent etching step, uniform removal of the unmodified covers at both surfaces occurs before the increased etching rate of the laser modified glass [36] leads to a separation when the etching radius exceeds the modification pitch at each depth within the sample. Figure 13 shows the symmetric edge that is produced with this revised processing strategy and the shifted focal line. The vertex of the curved height profile is positioned at the center of the glass sheet within the accuracy of the linearly determined focus position (±50 µm). The large pitch and etching radius leads to pronounced height modulations with an amplitude of up to 10 µm in horizontal cross section, which can be seen as periodic pattern in side view, see Fig. 13c).

5 Conclusion

We have demonstrated single pass perforation glass sheets with an Airy-Gauss beam. After a subsequent etching process it was possible to separate the glass pieces, and a convex edge was achieved. We found that the low focal contrast the Airy beam (in comparison, for example, to a Bessel beam) is a crucial limiting factor. Careful tuning of the laser parameters is necessary

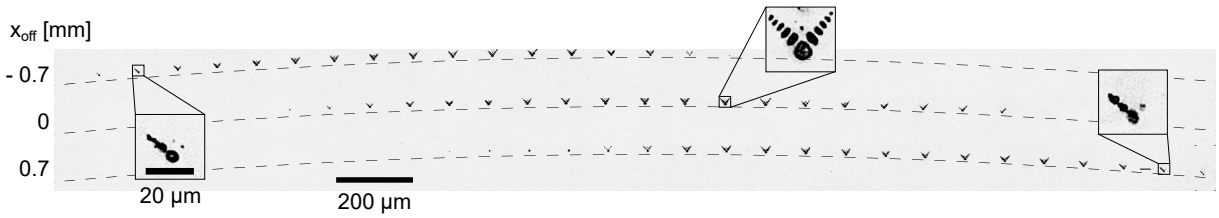

Fig. 11 Surface modifications for three scans along the z axis with different values of x_{off}. The focus position Δz is changed in steps of 10 µm from left to right respectively, so that the intensity distribution of the Airy beam is sampled at different propagation distances. A slight astigmatism can be seen for the tilted cases, as one Airy "leg" is longer at the far end of the propagation respectively.

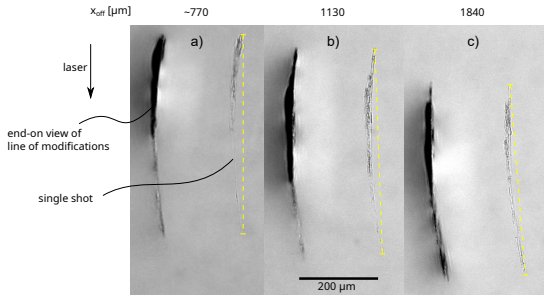

Fig. 12 Longitudinal cross section of volume modifications for varying offset x_{off} of the Gaussian input beam on the cubic phase mask ($w_0 = 5.3$ mm, $f = 10$ mm, 5 ps pulses). The dashed yellow lines connect the measured endpoints of each modifications. Note that the value for x_{off} in a) is a rough estimate due to a poorly defined initial state. A 4 pulse burst is chosen (in contrast to the 2 pulse burst used for the separation experiments) to increase the visibility of the volume modifications in the light microscopy image.

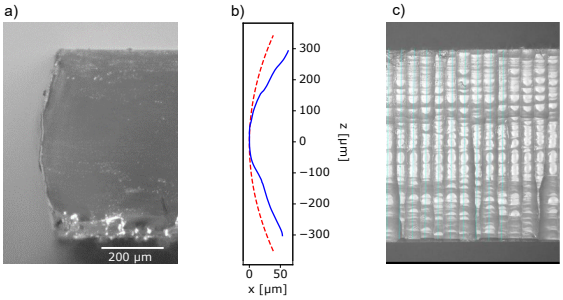

Fig. 13 Convex edge (a) resulting from the etching of in volume modifications with an Airy beam using a 10 mm diameter Gaussian input beam offset by $x_{\text{off}} = 770$ µm, f = 10mm, 2 pulse burst, 300 µJ burst energy, 5 ps. The average height profile (b, solid blue) measured by confocal light microscopy in side view of the convex edge (c) shows a stronger curvature than the theoretical Airy profile (dashed red) due to etching, similar to previous results [11].

to control the balance between surface and volume damage, in particular with respect to the side lobes of the Airy profile. Moreover, the permanent modifications that are produced by a focused Airy beam exhibit an asymmetric distribution of damage. This asymmetry increases with the pulse peak intensity and can be attributed to ignition of an electron plasma in the side lobes and a resulting shielding of the parts of the beam that feed the lower part of the focal line. We have demonstrated that this asymmetry can be compensated by tilting the Airy beam which we achieve by using an input beam with a lateral offset on the phase mask. By taking care to avoid unwanted surface or interaction effects we obtain a symmetric edge as a result of etching after Airy beam laser structuring of a 920 µm thick SCHOTT Borofloat® 33 sheet.

The etching process necessary for separation further reduced the achievable radius of curvature by almost a factor two, well beyond that of the Airy trajectory, which itself is limited by the trade-off between focus length and curvature. Nevertheless, for many industrial processes it would be favourable to achieve a clean separation with a rounded or bevelled edge by mechanical cleaving only. Such a mechanically cleaved edge was indeed recently produced with a modified Airy-Gauss beam [37], where in particular the contrast between main and side-lobes of the beam profile was improved. Other very recent attempts employed a multispot approach for edge shaping [38]. We expect that micromachining with accelerating beams will see further research activities in near future, because single pass curved glass cutting provides a fast, clean and versatile alternative to the conventional cutting and grinding methods, which does not only reduce costs but also enables more custom tailored solutions for industrial applications.

Acknowledgments. Simulations were performed using HPC resources from GENCI (Grants # A0070506129 and A0080507594). SS acknowledges support by the QNRF (Grant # NPRP 12S-0205-190047).

Declarations

Data underlying the results presented in this paper are not publicly available at this time but may be obtained from the authors upon reasonable request.

References

[1] Deubener, J., Helsch, G., Moiseev, A., Bornhöft, H.: Glasses for solar energy conversion systems. Journal of the European Ceramic Society **29**, 1203–1210 (2009). https://doi.org/10.1016/j.jeurceramsoc.2008.08.009

[2] Park, J.-S., Chae, H., Chung, H.K., Lee, S.I.: Thin film encapsulation for flexible AM-OLED: a review. Semiconductor Science and Technology **26**, 034001 (2011). https://doi.org/10.1088/0268-1242/26/3/034001

[3] Garner, S., Glaesemann, S., Li, X.: Ultra-slim flexible glass for roll-to-roll electronic device fabrication **116**, 403 (2014). https://doi.org/10.1007/s00339-014-8468-2

[4] Gattass, R.R., Mazur, E.: Femtosecond laser micromachining in transparent materials. Nature Photonics **2**(4), 219–225 (2008). https://doi.org/10.1038/nphoton.2008.47

[5] Hendricks, F., Matylitsky, V., Domke, M., Huber, H.P.: Time-resolved study of femtosecond laser induced micro-modifications inside transparent brittle materials. In: Frontiers in Ultrafast Optics: Biomedical, Scientific, and Industrial Applications XVI, vol. 9740, pp. 162–169 (2016). https://doi.org/10.1117/12.2214081. SPIE

[6] Herman, R.M., Wiggins, T.A.: Production and uses of diffractionless beams. J. Opt. Soc. Am. A **8**, 932–942 (1991). https://doi.org/10.1364/JOSAA.8.000932

[7] Mishchik, K., Beuton, R., Dematteo Caulier, O., Skupin, S., Chimier, B., Duchateau, G., Chassagne, B., Kling, R., Hönninger, C., Mottay, E., Lopez, J.: Improved laser glass cutting by spatio-temporal control of energy deposition using bursts of femtosecond pulses. Optics Express **25**(26), 33271 (2017). https://doi.org/10.1364/OE.25.033271

[8] Jenne, M., Flamm, D.l., Chen, K., Schäfer, M., Kumkar, M., Nolte, S.: Facilitated glass separation by asymmetric bessel-like beams. Optics Express **28**(5), 6552–6564 (2020). https://doi.org/10.1364/OE.387545

[9] Bergner, K., Müller, M., Klas, R., Limpert, J., Nolte, S., Tünnerman, A.: Scaling ultrashort laser pulse induced glass modifications for cleaving applications. Applied optics **57**(21), 5941–5947 (2018). https://doi.org/10.1364/AO.57.005941

[10] Feuer, A., Thomas, J.-U., Freitag, C., Weber, R., Graf, T.: Single-pass laser separation of 8 mm thick glass with a millijoule picosecond pulsed gaussian–bessel beam. Applied Physics A **125**(5), 1–6 (2019). https://doi.org/10.1007/s00339-019-2624-7

[11] Sohr, D., Thomas, J.U., Skupin, S.: Shaping convex edges in borosilicate glass by single pass perforation with an airy beam. Optics letters **46**(10), 2529–2532 (2021). https://doi.org/10.1364/OL.423788

[12] Berry, M.V., Balazs, N.L.: Nonspreading wave packets. American Journal of Physics **47**(3), 264–267 (1979). https://doi.org/10.1119/1.11855

[13] Siviloglou, G.A., Broky, J., Dogariu, A., Christodoulides, D.N.: Observation of accelerating airy beams. Physical Review Letters **99**(21), 213901 (2007). https://doi.org/10.1103/PhysRevLett.99.213901

[14] Yang, Z., Prokopas, M., Nylk, J., Coll-Lladó, C., Gunn-Moore, F.J., Ferrier, D.E.K., Vettenburg, T., Dholakia, K.: A compact airy beam light sheet microscope with a tilted cylindrical lens. Biomedical Optics Express **5**(10), 3434–3442 (2014). https://doi.org/10.

1364/BOE.5.003434

[15] Panagiotopoulos, P., Papazoglou, D.G., Couairon, A., Tzortzakis, S.: Sharply autofocused ring-airy beams transforming into non-linear intense light bullets. Nature Communications **4**, 2622 (2013). https://doi.org/10.1038/ncomms3622

[16] Mathis, A., Courvoisier, F., Froehly, L., Furfaro, L., Jacquot, M., Lacourt, P.A., Dudley, J.M.: Micromachining along a curve: Femtosecond laser micromachining of curved profiles in diamond and silicon using accelerating beams. Applied Physics Letters **101**(7), 071110 (2012). https://doi.org/10.1063/1.4745925

[17] Froehly, L., Courvoisier, F., Mathis, A., Jacquot, M., Furfaro, L., Giust, R., Lacourt, P.A., Dudley, J.M.: Arbitrary accelerating micron-scale caustic beams in two and three dimensions. Optics express **19**(17), 16455–16465 (2011). https://doi.org/10.1364/OE.19.016455

[18] Polynkin, P., Kolesik, M., Moloney, J.V., Siviloglou, G.A., Christodoulides, D.N.: Curved plasma channel generation using ultraintense airy beams. Science **324**(5924), 229–232 (2009). https://doi.org/10.1126/science.1169544

[19] Efremidis, N.K., Chen, Z., Segev, M., Christodoulides, D.N.: Airy beams and accelerating waves: an overview of recent advances. Optica **6**(5), 686 (2019). https://doi.org/10.1364/OPTICA.6.000686

[20] Papazoglou, D.G., Suntsov, S., Abdollahpour, D., Tzortzakis, S.: Tunable intense airy beams and tailored femtosecond laser filaments. Physical Review A **81**(6), 061807 (2010). https://doi.org/10.1103/PhysRevA.81.061807

[21] Raghwinder S. Grewal, Anirban Ghosh, G. K. Samanta: Simultaneous generation of high-power, ultrafast 1d and 2d airy beams and their frequency-doubling characteristics. Optics Letters **43**(16), 3957–3960 (2018). https://doi.org/10.1364/OL.43.003957

[22] Gottmann, J.: Microcutting and hollow 3d microstructures in glasses by in-volume selective laser-induced etching (isle). Journal of Laser Micro/Nanoengineering **8**(1), 15–18 (2013). https://doi.org/10.2961/jlmn.2013.01.0004

[23] Matsuo, S., Sumi, H., Kiyama, S., Tomita, T., Hashimoto, S.: Femtosecond laser-assisted etching of pyrex glass with aqueous solution of koh. Applied surface science **255**(24), 9758–9760 (2009). https://doi.org/10.1016/j.apsusc.2009.04.065

[24] Bergé, L., Skupin, S., Nuter, R., Kasparian, J., Wolf, J.P.: Ultrashort filaments of light in weakly ionized, optically transparent media. Reports on Progress in Physics **70**, 1633 (2007)

[25] Dematteo Caulier, O., Mishchik, K., Chimier, B., Skupin, S., Bourgeade, A., Javaux Léger, C., Kling, R., Hönninger, C., Lopez, J., Tikhonchuk, V., Duchateau, G.: Femtosecond laser pulse train interaction with dielectric materials. Applied Physics Letters **107**, 181110 (2015)

[26] Keldysh, L.V.: Ionization in the field of a strong electromagnetic wave. Sov. Phys. JETP **20**(5), 1307–1314 (1965)

[27] Audebert, P., Daguzan, P., Dos Santos, A., Gauthier, J., Geindre, J., Guizard, S., Hamoniaux, G., Krastev, K., Martin, P., Petite, G., *et al.*: Space-time observation of an electron gas in si o 2. Physical Review Letters **73**(14), 1990 (1994). https://doi.org/10.1103/PhysRevLett.73.1990

[28] Mauclair, C., Mermillod-Blondin, A., Mishchik, K., Bonse, J., Rosenfeld, A., Colombier, J.P., Stoian, R.: Excitation and relaxation dynamics in ultrafast laser irradiated optical glasses. High Power Laser Science and Engineering **4**, 1065 (2016). https://doi.org/10.1017/hpl.2016.45

[29] Liu, W., Petit, S., Becker, A., Aközbek, N., Bowden, C.M., Chin, S.L.: Intensity clamping of a femtosecond laser pulse in condensed matter. Optics Communications

202(1), 189–197 (2002). https://doi.org/10.1016/S0030-4018(01)01698-4

[30] A. Schmitt-Sody, H. G Kurz, L. Bergé, S. Skupin, P. Polynkin: Picosecond laser filamentation in air. New Journal of Physics **18**(9), 093005 (2016). https://doi.org/10.1088/1367-2630/18/9/093005

[31] Eppelt, U., Russ, S., Hartmann, C., Sun, M., Siebert, C., Schulz, W.: Diagnostic and simulation of ps-laser glass cutting. In: International Congress on Applications of Lasers & Electro-Optics, vol. 2012, pp. 835–844 (2012). Laser Institute of America

[32] Hu, Y., Siviloglou, G.A., Zhang, P., Efremidis, N.K., Christodoulides, D.N., Chen, Z.: Self-accelerating airy beams: Generation, control, and applications. In: Chen, Z., Morandotti, R. (eds.) Nonlinear Photonics and Novel Optical Phenomena. Springer Series in Optical Sciences, vol. 170, pp. 1–46. Springer New York, New York, NY (2012)

[33] Saleh, B.E.A., Teich, M.C.: Fundamentals of Photonics. Wiley Series in Pure and Applied Optics. Wiley-Interscience, Hoboken, NJ (2001). https://doi.org/10.1002/0471213748

[34] Cottrell, D.M., Davis, J.A., Hazard, T.M.: Direct generation of accelerating airy beams using a 3/2 phase-only pattern. Optics Letters **34**(17), 2634–2636 (2009). https://doi.org/10.1364/OL.34.002634

[35] Boling, N.L., Crisp, M.D., Dubé, G.: Laser induced surface damage. Applied Optics **12**(4), 650 (1973). https://doi.org/10.1364/ao.12.000650

[36] Bischof, D., Kahl, M., Michler, M.: Laser-assisted etching of borosilicate glass in potassium hydroxide. Optical Materials Express **11**(4), 1185 (2021). https://doi.org/10.1364/OME.417871

[37] Ungaro, C., Liu, A.: Single-pass cutting of glass with a curved edge using ultrafast curving bessel beams and oblong airy beams. Optics & Laser Technology **144**, 107398 (2021). https://doi.org/10.1016/j.optlastec.2021.107398

[38] Flamm, D., Kaiser, M., Feil, M., Kahmann, M., Lang, M., Kleiner, J., Hesse, T.: Protecting the edge: Ultrafast laser modified c-shaped glass edges. Journal of Laser Applications **34**(1), 012014 (2022). https://doi.org/10.2351/7.0000592